Title
Bandgap engineering in semiconductor alloy nanomaterials with widely tunable compositions

Journal
Nature Reviews Materials, 2(12)

ISSN
2058-8437

Authors
Peidong Yang, CZN
Dou, L
Yang, P

Publication Date
2017-10-31

DOI
10.1038/natrevmats.2017.70

Peer reviewed

Bandgap engineering in semiconductor alloy nanomaterials with widely tunable compositions

Cun-Zheng Ning[1,2], Letian Dou[3–5] and Peidong Yang[3,4,6]

Abstract | Over the past decade, tremendous progress has been achieved in the development of nanoscale semiconductor materials with a wide range of bandgaps by alloying different individual semiconductors. These materials include traditional II–VI and III–V semiconductors and their alloys, inorganic and hybrid perovskites, and the newly emerging 2D materials. One important common feature of these materials is that their nanoscale dimensions result in a large tolerance to lattice mismatches within a monolithic structure of varying composition or between the substrate and target material, which enables us to achieve almost arbitrary control of the variation of the alloy composition. As a result, the bandgaps of these alloys can be widely tuned without the detrimental defects that are often unavoidable in bulk materials, which have a much more limited tolerance to lattice mismatches. This class of nanomaterials could have a far-reaching impact on a wide range of photonic applications, including tunable lasers, solid-state lighting, artificial photosynthesis and new solar cells.

[1]*Department of Electronic Engineering, Tsinghua University, Beijing 100084, China.*
[2]*School of Electrical, Computer and Energy Engineering, Arizona State University, Tempe, Arizona 85287, USA.*
[3]*Department of Chemistry, University of California, Berkeley, California 94720, USA.*
[4]*Materials Sciences Division, Lawrence Berkeley National Laboratory, Berkeley, California 94720, USA.*
[5]*Present address: Davidson School of Chemical Engineering, Purdue University, West Lafayette, Indiana 47907, USA.*
[6]*Department of Materials Science and Engineering, University of California, Berkeley, California 94720, USA.*

Correspondence to C.-Z.N. and P.Y.
cning@asu.edu; p_yang@berkeley.edu

doi:10.1038/natrevmats.2017.70
Published online 31 Oct 2017

In a semiconductor, the bandgap is arguably the most critical parameter for almost all applications involving photon absorption or emission, such as solar cells, solid-state lighting, detectors, displays, sensors, lasers and photocatalytic reactions. In solar cells, only photon energies close to the bandgap energy can be converted into electricity: higher-energy photons lose energy by thermalization and phonon generation, whereas lower-energy photons are simply transmitted through the solar cell. Thus, efficient solar cells require the combined use of multiple semiconductors with various bandgaps. Multicolour or multiwavelength photodetectors and on-chip spectrometers would be enabled by semiconductors with a larger range of bandgaps. In solid-state lighting, illumination and displays, direct red–green–blue (RGB) or multicolour emission is desired to achieve, in the long term, high efficiency and low-cost fabrication. This requires semiconductors with bandgaps in the range 1.77–3.1 eV. For solid-state lighting, it is still impossible to realize all-semiconductor white light-emitting diodes (LEDs) from a single monolithic semiconductor to enable light sources with high luminosity and long lifetimes. The conventional approaches still use non-semiconductor phosphors combined with a semiconductor emitter for the generation of white light, which results in inefficient and low-quality lighting.

Revolutionary advances are expected if it becomes possible to achieve semiconductors with any desired bandgap that can be tailored for specific applications. Such dream materials would also enable many new applications. Not all bandgaps are naturally available through the direct synthesis of elemental or binary individual semiconductors; one common approach to creating otherwise non-existent bandgaps is to alloy two or more semiconductors with different bandgaps. By controlling the alloy composition, all the bandgaps between those of the constituent semiconductors can in principle be realized. However, the range of bandgaps that can be achieved in high-quality single-crystal alloys is limited in practice by the strict requirement of lattice matching in planar epitaxial growth (in addition to chemical solubility or miscibility): the lattice constant of the material to be grown has to be very similar to that of the substrate (FIG. 1). Owing to the limited availability of substrates (commonly available substrates are indicated by dashed black lines in FIG. 1) and the lattice mismatch issue, the range of achievable bandgaps is severely limited. A small tolerance to mismatch (for example, a 1% mismatch with respect to a GaAs substrate, as shown by the red shading in FIG. 1) enables the achievement of only a small range of bandgaps (~0.7 eV for ZnHgS), whereas a larger tolerance to mismatch would enable a much larger range of bandgaps (~2.5 eV for ZnHgS for a 3% mismatch, green shading in FIG. 1) on the same substrate.

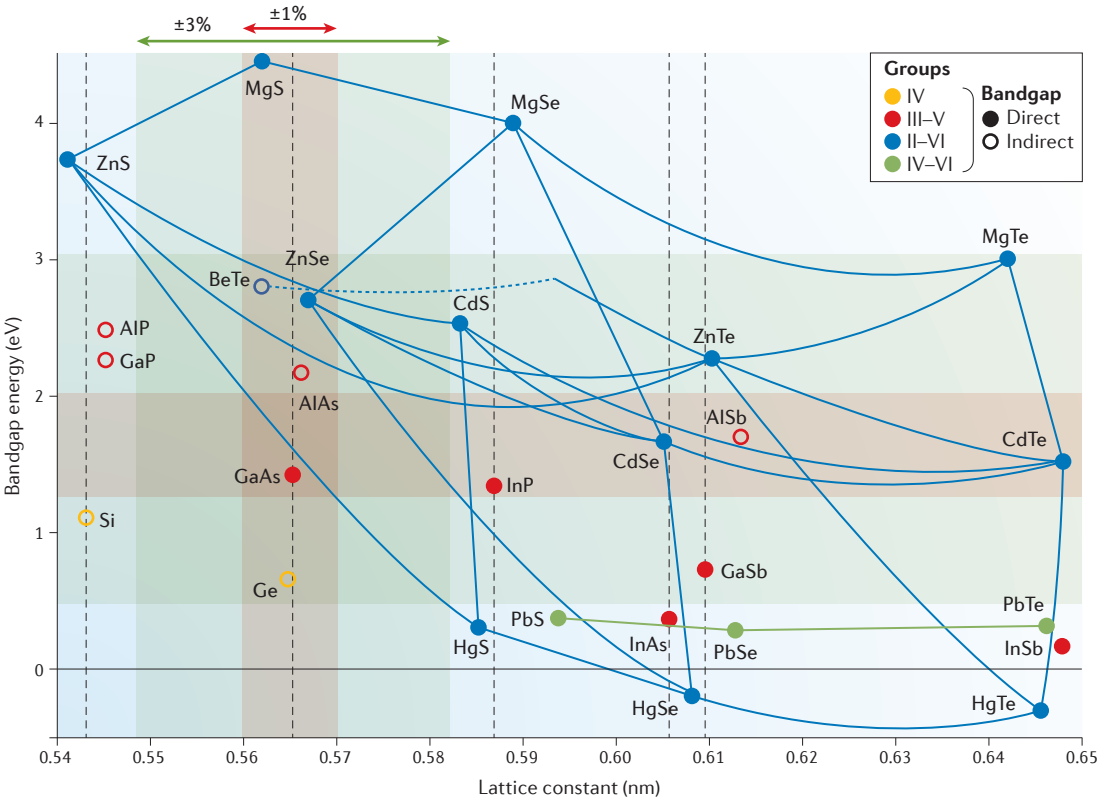

Figure 1 | **Bandgaps and lattice constants for typical semiconductors and their alloys.** Filled and unfilled circles indicate, respectively, direct and indirect bandgap materials, and solid and dashed connecting lines indicate, respectively, direct and indirect alloys. For simplicity, only group II–VI and IV–VI alloys are shown. The five black dashed vertical lines indicate commonly used substrates for the epitaxial growth of materials: Si, GaAs, InP, InAs and GaSb. The ranges of available lattice constants and corresponding bandgaps for a 1% and 3% lattice mismatch with GaAs are indicated by the red and green shaded areas, respectively. High-quality materials with a few per cent of mismatch can be readily grown at the nanoscale, leading to a large range of bandgaps in nanomaterials.

The effect of lattice mismatch on epitaxial growth is illustrated in FIG. 2, which shows the relationship between the critical thickness (the thickness above which significant dislocations are introduced) and lateral size of an epitaxial semiconductor disk for different lattice mismatches with the substrate[1]. The larger the lattice mismatch and the lateral size of the material, the smaller the critical thickness. For conventional planar epitaxial growth of thin films such as quantum-well structures, reaching a meaningful thickness (>10 nm) requires the lattice mismatch to be smaller than 1% to grow high-quality single crystals. This is the fundamental reason why planar epitaxial crystal growth can produce only a limited range of bandgaps. FIGURE 2 also provides an important hint for how to expand the range of lattice mismatches (and thus the range of bandgaps). If materials with smaller cross sections (a radius <100 nm) are grown, they can reach any thickness, even for lattice mismatches as large as 3–7%. The larger tolerance to lattice mismatch at the nanoscale allows us to substantially expand the range of achievable energy bandgaps and provides many opportunities for growing materials in new alloy composition ranges for both materials research and novel device applications. Such large tolerance to lattice mismatch also enables the growth of very dissimilar materials into monolithic heterostructures. Moreover, lattice-mismatched structures at the nanoscale are likely to respond elastically to dissimilar expansions under thermal stress without breaking the structure.

The large tolerance to lattice mismatch was one of the main drivers in the development of nanoscale materials in the past decade. It has created unprecedented opportunities for growing semiconductor alloys with almost arbitrary compositions, on a substrate or in a single monolithic piece, with an extraordinarily large range of bandgaps on the order of several eV instead of 10s of meV. These materials include traditional II–VI and III–V semiconductors and their alloys in nanowire or nanosheet forms, inorganic and hybrid perovskites, and 2D materials. These almost arbitrary alloys with almost arbitrary bandgaps are promising for applications in a wide wavelength range and will have a far-reaching impact on photonic applications.

In this article, we review the progress made over the past decade in exploring these advantageous properties of nanomaterials and their impact on materials research and device applications. In the introduction, we presented a general background on semiconductor alloys and the bandgap dependence on alloy composition, emphasizing the limitations of planar epitaxial growth.

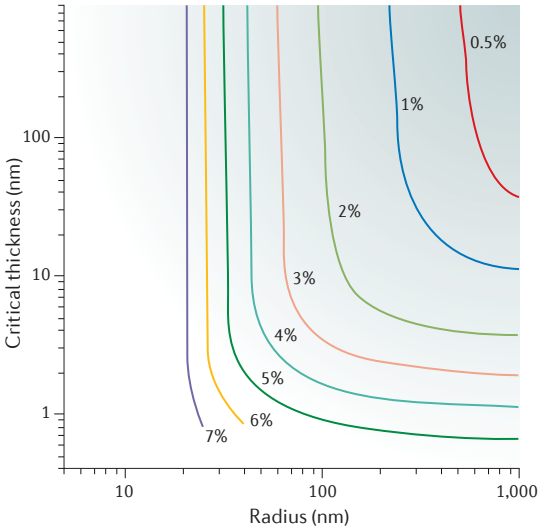

Figure 2 | **Effect of lattice mismatch on epitaxial growth.** The critical thickness of a semiconductor disk epitaxially grown on a substrate is shown as a function of the lateral size of the disk (its radius) for different percent mismatches between the lattice constant of the substrate and that of the disk. Adapted with permission from REF. 1, American Physical Society.

We have also discussed the quantitative advantages in terms of tolerance to lattice mismatch afforded by materials with characteristic scales of 10–100 nm. The focus of this Review is on the growth and synthesis of nanomaterials with a wide range of alloy compositions, including II–VI and III–V semiconductors, halide perovskites and 2D monolayer transition metal dichalcogenides (TMDCs). Owing to the vast amount of literature, rather than trying to cover the entire field, we concentrate on alloy composition and bandgap flexibility. We conclude with an overview of the unique applications enabled by these new material platforms and the future perspectives for the exploration of the limits of 'arbitrary alloying' and its potential for new device applications.

Epitaxial growth of nanowires

In the epitaxial growth of nanowires from a crystalline substrate, the crystalline planes of the substrate can be used to control the orientation of the nanowires. This enables great control over the orientation and large-scale uniformity of the nanowires, which is important for the fabrication of large-scale devices. Because nanowire epitaxy implies a larger tolerance to lattice mismatch compared with thin-film (planar) epitaxy, as discussed above, it enables materials studies and device applications that are impossible with planar epitaxy. Thus, the epitaxial growth of nanowires has generated considerable progress in several areas, including the achievement of the largest reported lattice mismatch of up to 10%[2,3] and the growth of many III–V compounds and their alloys on Si, which is a tremendously important area for Si photonics owing to the prevailing role played by Si in microelectronics and to the lack of efficient light-emitting materials based on Si. Selected-area epitaxy (SAE) is one of the most straightforward extensions of planar epitaxy for the growth of nanowires. Some particularly interesting examples are discussed in this section.

Metal-catalysed epitaxial growth on III–V substrates. One of the early examples demonstrating the tolerance of nanowires to large mismatches is the growth, by chemical beam epitaxy, of heterostructured nanowires with alternating InAs and InP segments[4]; the mismatch between the two materials is greater than 3%. This heterostructure also exemplifies the opportunities provided by nanowire technology, as the InAs/InP interface could not be studied before owing to the inability to produce high-quality interfaces resulting from the large mismatch. More recently, GaAsP and AlGaP alloy nanowires were grown on a GaP(111) substrate in their wurtzite phases[5], enabling the emitted wavelength to be tuned across the range 555–690 nm. Vapour–liquid–solid (VLS) growth of $GaAs_{1-x}Sb_x$ nanowires was demonstrated with Au catalysts on a GaAs(111)B substrate by means of metal–organic vapour phase epitaxy (MOVPE)[6]. Incorporation of Sb was tuned over a broad range (x was changed from 0.09 to 0.6) solely by changing the AsH_3 flow.

III–V nanowires on Si substrates. The monolithic integration of III–V semiconductors on Si substrates has been a long-standing goal. The growth of III–V semiconductor nanowires on Si provides the best opportunity to demonstrate the uniquely large tolerance to lattice mismatches of nanomaterials. The success of this approach is having a tremendous impact on many technologies in which light-emitting III–V compounds can be integrated with the Si technology that dominates the microelectronics industry. Thus, this approach has attracted much attention in device-oriented research. The earliest attempt[7] was the growth of GaP, GaAs and InP on Si. GaP was the natural first choice owing to the close lattice matching with Si. GaP nanowires were first demonstrated on Si(111) and Si(100) with a VLS-based MOVPE approach, and to demonstrate light generation on Si, segments of GaP wires were replaced by light-emitting GaAsP with up to 70% As. Whereas the successful growth of GaP on Si was not surprising, the epitaxial growth of GaAs and InP nanowires on Si(111) demonstrated[7] the true advantage of nanowire growth in III–V–Si integration, owing to the large lattice mismatches of 4% (for GaAs) and 8% (for InP). The growth of III–V semiconductors and their alloys on Si has attracted much attention ever since. The rapidly increasing understanding and control of the growth process has led to efforts to develop applications in electronics and photonics using this attractive platform[8–14].

InAs is one of the III–V materials with the largest mismatch with Si (more than 10%). Thus, the growth of InAs nanowires on Si showcases the success of the nanowire approach. Several groups[2,3] have successfully demonstrated epitaxial growth of InAs nanowires on Si(111) using SAE and metal–organic chemical vapour deposition (MOCVD), obtaining great control over the wire orientation without the need to use foreign metals as catalysts. The growth of InGaAs tapered pillars with

12–20% In on Si(111) was later demonstrated at low temperature, which is compatible with the complementary metal–oxide–semiconductor (CMOS) technology[15]. A much larger range of compositions (almost the entire range between GaAs and InAs) was achieved on Si substrates, showing predominantly a zinc-blende phase in In-rich compositions and a wurtzite phase in Ga-rich compounds. GaAs nanowires were epitaxially grown[16] on Si(001) and Si(111) substrates with a Au catalyst by use of solid-source molecular beam epitaxy. Almost all the GaAs nanowires were grown along the <111> directions on both Si substrates. X-ray diffraction and transmission electron microscopy (TEM) analysis showed that the GaAs <111> nanowires had a mixed wurtzite and zinc-blende structure.

Growth of III–nitrides on Si is an active area of research in the planar-epitaxy community and is also promising for nanowire epitaxy. The large lattice mismatch tolerance enabled the growth of complex InGaN structures on Si(001), including wells and barriers with different In compositions along the nanowires[17,18] and the demonstration of visible lasers[17]. InGaN nanowires with varying In content resulting in quantum wells along the radial direction were also demonstrated[19]. Some recent reviews provide extensive discussions of nanowires of InGaN (REFS 20,21) and AlGaN (REF. 22) alloys.

Selective area epitaxy. SAE is a technique based on the patterned exposure and masking of a single-crystal substrate by a thin layer of amorphous material so that the subsequent crystal growth is initiated from only the exposed portions of the crystal. SAE is especially suited for the growth of nanowires when the exposed areas are on the order of the desired nanowire diameter, typically from 10s to 100s of nm. The patterning of the amorphous layer is often carried out using electron beam lithography (EBL), which raises the cost of the SAE approach. SAE substrates can be quite mismatched with the nanowire materials, and both III–V and Si substrates have been used successfully for the growth of III–V nanowires, with the nanowire orientation controlled by the underlying crystal substrate.

Vertical arrays of $In_xGa_{1-x}P$ nanowires were grown[23] using SAE on an n-doped (111)A InP substrate, both with and without metal particles as catalysers; a 25-nm-thick SiO_x film was used to generate the SAE pattern using EBL. Characterization of the nanowires showed a pure wurtzite phase with very few stacking faults. Both the growth temperature and the Ga/precursor ratio can be used to control the alloy composition of the nanowires, with photoluminescence (PL) emission peaks varying from those of pure InP (870 nm or 1.42 eV for the wurtzite structure) to 800 nm. The MOVPE-based SAE growth of nanowires on Si is discussed extensively in REF. 24.

$In_xGa_{1-x}P$ alloy nanowires have also been studied, mostly using MOCVD[23,25,26] but also other low-cost methods such as the solution–liquid–solid[27] or chemical vapour deposition (CVD) method[28]. MOCVD mostly produced nanowires of mixed zinc-blende and wurtzite phases with limited composition ranges, whereas the solution-based method has produced pure-phase alloys in the full composition range from InP to GaP, showing a bandgap dependence on the alloy composition similar to that expected in the bulk. Such materials could prove important for applications in solar cells because $In_xGa_{1-x}P$ alloys have two important bandgaps for middle- and high-gap solar cells.

Spatial composition and bandgap control

Spatial composition grading on a single substrate. Perhaps the best illustration of bandgap flexibility in alloys of nanostructured semiconductors is the realization of a wide range of bandgaps on a single substrate in a single growth run[29], which is impossible in traditional planar epitaxial growth. Several approaches based on CVD can be used to this end[4,30–32] (FIG. 3a). One possibility is using two source materials placed in two separate minitubes at different axial locations (FIG. 3a). Owing to the temperature profile along the axial direction, moving the sources changes their sublimation temperature and thus determines the relative amount of the two gas-phase source materials on the substrate downstream. In addition, the spatial distribution of the elemental composition on the substrate can also be changed by varying the separation between the two minitubes. This is known as the source material gradient method and was first implemented for the growth of an InGaN alloy[33]. One advantage of this method is that it provides a range of possible In/Ga ratios, allowing the simultaneous testing of a range of compositions and growth conditions, which is the essence of combinatorial chemistry. As a result, InGaN alloys in the full composition range from pure GaN to InN were grown for the first time; this was important because it demonstrated that there is apparently no composition miscibility gap, at least in the nanowire form. The PL and absorption spectra and the bandgaps for different alloy compositions of this material as a function of In content are shown in FIG. 3b.

Complementary to the source elemental gradient approach is the temperature gradient method, which is based on the fact that the alloy composition also varies in response to non-uniform temperatures on the substrate[34,35,36]. In this approach, the substrate is placed horizontally and the two source materials are both placed in the main tube (FIG. 3a); the temperature at the two ends of the substrate can be controlled by adjusting the temperature profile. In particular, the temperature profile can be optimized such that the temperature at the two ends of the substrate favours the growth of the two binary compounds (S1 and S2), whereas the temperature at intermediate locations favours alloys of composition $S1_xS2_{1-x}$. The temperature gradient approach was used to grow CdSSe alloys, realizing the entire emission spectrum from green to red on a single chip[36] and continuous spatial tunable lasing with wavelength tuning over a range of 200 nm (FIG. 3c).

The source elemental gradient method and temperature gradient method have proved useful, but they have obvious deficiencies. It is therefore natural to combine them in a single setup. Tilting the substrate is enough to take advantage of both the temperature and the source material gradient, obtaining the so-called dual gradient

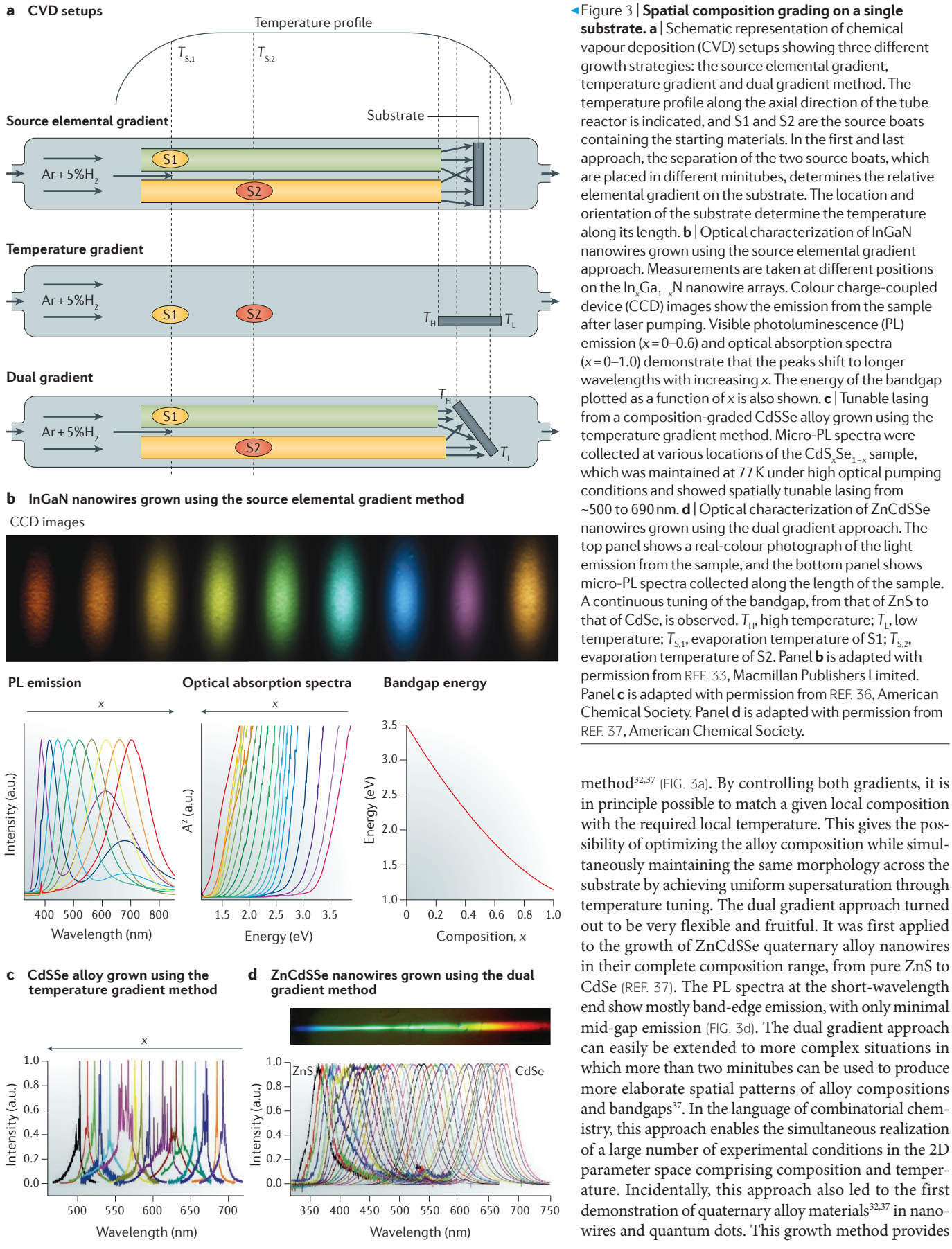

◂Figure 3 | **Spatial composition grading on a single substrate. a** | Schematic representation of chemical vapour deposition (CVD) setups showing three different growth strategies: the source elemental gradient, temperature gradient and dual gradient method. The temperature profile along the axial direction of the tube reactor is indicated, and S1 and S2 are the source boats containing the starting materials. In the first and last approach, the separation of the two source boats, which are placed in different minitubes, determines the relative elemental gradient on the substrate. The location and orientation of the substrate determine the temperature along its length. **b** | Optical characterization of InGaN nanowires grown using the source elemental gradient approach. Measurements are taken at different positions on the $In_xGa_{1-x}N$ nanowire arrays. Colour charge-coupled device (CCD) images show the emission from the sample after laser pumping. Visible photoluminescence (PL) emission ($x = 0–0.6$) and optical absorption spectra ($x = 0–1.0$) demonstrate that the peaks shift to longer wavelengths with increasing x. The energy of the bandgap plotted as a function of x is also shown. **c** | Tunable lasing from a composition-graded CdSSe alloy grown using the temperature gradient method. Micro-PL spectra were collected at various locations of the CdS_xSe_{1-x} sample, which was maintained at 77 K under high optical pumping conditions and showed spatially tunable lasing from ~500 to 690 nm. **d** | Optical characterization of ZnCdSSe nanowires grown using the dual gradient approach. The top panel shows a real-colour photograph of the light emission from the sample, and the bottom panel shows micro-PL spectra collected along the length of the sample. A continuous tuning of the bandgap, from that of ZnS to that of CdSe, is observed. T_H, high temperature; T_L, low temperature; $T_{S,1}$, evaporation temperature of S1; $T_{S,2}$, evaporation temperature of S2. Panel **b** is adapted with permission from REF. 33, Macmillan Publishers Limited. Panel **c** is adapted with permission from REF. 36, American Chemical Society. Panel **d** is adapted with permission from REF. 37, American Chemical Society.

method[32,37] (FIG. 3a). By controlling both gradients, it is in principle possible to match a given local composition with the required local temperature. This gives the possibility of optimizing the alloy composition while simultaneously maintaining the same morphology across the substrate by achieving uniform supersaturation through temperature tuning. The dual gradient approach turned out to be very flexible and fruitful. It was first applied to the growth of ZnCdSSe quaternary alloy nanowires in their complete composition range, from pure ZnS to CdSe (REF. 37). The PL spectra at the short-wavelength end show mostly band-edge emission, with only minimal mid-gap emission (FIG. 3d). The dual gradient approach can easily be extended to more complex situations in which more than two minitubes can be used to produce more elaborate spatial patterns of alloy compositions and bandgaps[37]. In the language of combinatorial chemistry, this approach enables the simultaneous realization of a large number of experimental conditions in the 2D parameter space comprising composition and temperature. Incidentally, this approach also led to the first demonstration of quaternary alloy materials[32,37] in nanowires and quantum dots. This growth method provides

an unprecedented alloy library with a wide variety of quaternary compositions in the 2D space spanned by the four binaries ZnS, ZnSe, CdS and CdSe (REF. 37).

Spatial composition control within a single nanostructure. Considering the successful demonstration of the possibility of controlling the alloy composition and bandgap on a single substrate, it is tempting to ask if similar control can be achieved within a single nanostructure, such as a nanowire, nanosheet or nanobelt. This is possible owing to the large lattice mismatch tolerance at the nanoscale that enables the growth of alloys with very different compositions and lattice parameters in a single nanostructure. The temperature dependence of the alloy composition in the final product is key to realizing variations in composition within a wire[38]. The position of the substrate is changed to expose it to different temperatures during growth; this led to ZnCdSSe wires with axial composition control within individual wires[39]. The changes in composition and bandgap can be either continuous or abrupt (as is the case for the InAs/InP axial heterostructures demonstrated earlier[4]). Emission in the visible range was realized using CdS/CdSe nanowires, and these axial heterostructures were later extended to CdPbS (REF. 30). The CdSe/CdS nanowire structures, which were composed of two segments, produced the first demonstration of dual red–green lasing in a single monolithic structure[40] when the wide-gap end was rolled up to form a 'q' shape. This strategy to grow segmented nanowires was also adopted to grow segmented nanosheets[41]: first, a rectangular sheet of CdS was grown; then, the source was switched to CdSe and the substrate position was changed to be exposed to the right temperature to grow the CdSe segment. In this way, a structure with parallel segments containing a green-emitting inner region and a red-emitting outer region was obtained. The thickness of these structures is of the order of 100–200 nm, enough to support slap modes in the vertical direction for red and green wavelengths[41]. These parallel structures produce simultaneous lasing in red and green more easily than segmented nanowires.

The successful demonstration of simultaneous red and green lasing and the associated colour tuning naturally led to attempts to realize simultaneous RGB lasing, or white lasing. Although simultaneous spontaneous emissions in RGB have been achieved in axial multisegment nanowires[38], it is difficult for such nanowires to support RGB lasing owing to absorption of the short-wavelength emissions by the narrow-gap segments. A direct extension of the multisegment nanosheets enabling red–green lasers[41] would be the addition of a blue-emitting segment. For CdSSe alloys, the most straightforward addition would be a segment of a ZnS-rich alloy. Unfortunately, such a direct addition proved to be challenging. The reason is that most wide-gap materials, such as ZnS, have low vapour pressure. In VLS–CVD growth, such materials tend to grow into nanowires or nanobelts with much higher aspect ratios than those of nanosheets of CdSe or CdS reported in REF. 41. Thus, there is an incompatibility between the desired morphology (nanosheet) and alloy composition, which cannot both be achieved in a single growth step. Here again, the flexibility of nanoscale materials was key to solving the problem, and an indirect two-step process resulted in the desired morphology and composition[42,43] (FIG. 4). The substrate was attached to a movable magnetic support so that it could be exposed to different temperatures and supersaturation levels[38] (FIG. 4a). The key was to grow a red-emitting (CdSe-rich alloy) nanosheet first. Then, the substrate position was changed and, at the same time, ZnS was moved into the heating zone, which allowed simultaneous anion and cation exchanges, and the replacement of Cd and Se by Zn and S, respectively. The reaction time was controlled so that the dual ion-exchange process continued until the right compositions (Zn/Cd and S/Se ratios) were achieved and the originally red-emitting nanosheet started emitting blue light. The high quality of the PL images and spectra (FIG. 4c,d) shows that the dual ion-exchange process is uniform, owing to the nanoscale size of the structures; the growth of these monolithic nanosheets with a lattice mismatch of more than 6% was possible owing to the small thickness of the structure (100–200 nm). The high quality of the material is also highlighted by the ability of each segment to support lasing in red, green and blue sequentially or simultaneously to produce white light (FIG. 4e,f). Thus, the unique properties of nanoscale materials allowed the first realization of a white laser[9] in a single monolithic device.

Alloys and heterostructures of 2D TMDCs

2D TMDCs have received substantial attention recently owing to their unique optical, electronic and spintronic properties. Such materials also offer unique opportunities for alloy and bandgap engineering. Owing to their chemical inertness in the vertical direction, alloy and bandgap engineering of 2D TMDCs occur mostly within the plane of the layers. As discussed, the large tolerance to lattice mismatches in nanomaterials stems from their small transverse sizes (FIG. 2). For monolayer TMDCs, the tolerance for lateral heterostructures or alloy composition changes is the largest possible, as 2D materials have the smallest possible size in the transverse direction. Therefore, such materials offer the ultimate playground for alloy composition and bandgap engineering; the alloy stability and composition miscibility for a class of 2D TMDCs was recently studied[44]. The largest tolerance to mismatches was found in the abrupt heterojunctions of dissimilar TMDCs and, upon alloying different TMDCs, for gradually changing alloy compositions. A comprehensive review is provided in REF. 45.

One of the direct methods for the growth of alloy TMDCs involves the simultaneous provision of two chalcogen elements together with the transition metal oxide in a CVD reactor, or of two binary bulk TMDCs, similar to the growth method in the lowest panel of FIG. 3a; S1 and S2 would be, for example, MoS_2 and $MoSe_2$ (REF. 46). By changing the evaporation temperatures $T_{S,1}$ and $T_{S,2}$, the S/Se ratio can be changed. A $MoS_{2(1-x)}Se_{2x}$ alloy with x as high as 0.4 was achieved with this process. Furthermore, similar to the temperature gradient effects discussed above, a weak dependence of the composition on temperature was observed, with lower temperatures

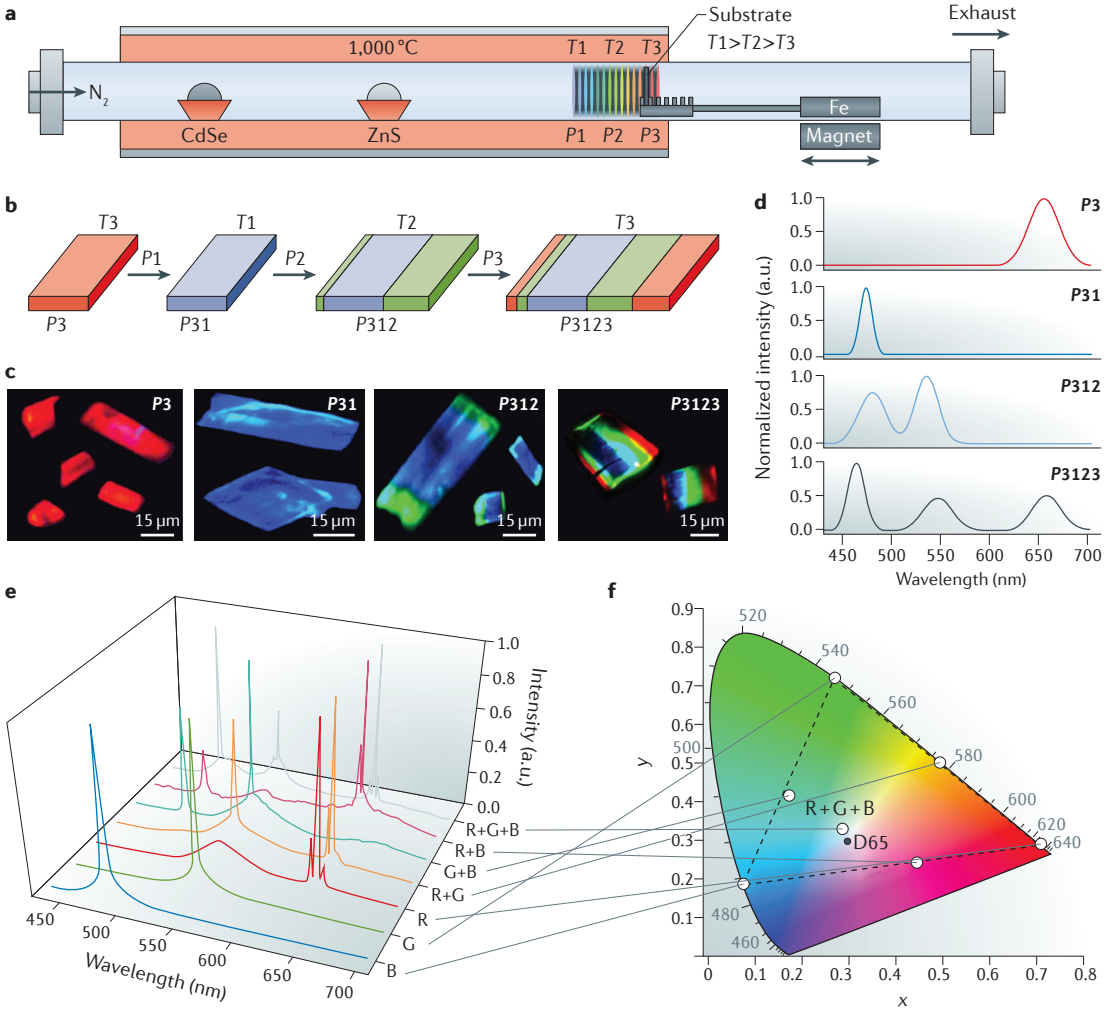

Figure 4 | **Growth and characterization of multisegment nanosheets for simultaneous lasing in red, green and blue.** **a** | The schematic setup shows that the substrate can be moved to different locations with different temperatures (*T*) and positions (*P*) for the growth of multisegment nanosheets. **b** | The schematic illustrates the segments constituting the nanosheet and the colour of each segment, showing the emitted colour after successive growth steps. **c** | Real-colour photoluminescence (PL) images acquired after each growth step. **d** | PL spectra acquired after each growth step. **e,f** | PL spectra recorded under various individual pumping conditions inducing lasing in one, two or all three segments and the corresponding colours (white dots). The final spectrum is represented by the central white dot, which is close to the white standard D65. R, G and B correspond to red, green and blue, respectively. Adapted with permission from REF. 42, Macmillan Publishers Limited.

favouring Se incorporation. The range of compositions was later extended to $x = 1$ using a similar setup and growth strategy[47].

Controllable sulfurization of monolayer diselenides or selenization of monolayer disulfides offers a straightforward means of creating monolayer alloys with controllable compositions. Selenization[48] of monolayers of MoS_2 pre-grown in a CVD tube furnace at 600, 700, 800 or 900 °C produced alloys of $MoS_{2(1-x)}Se_{2x}$ with PL peaks at 668, 726, 768 and 790 nm, respectively, indicating a near complete change from a pure diselenide to pure disulfide composition only by controlling the selenization temperature.

Another method to produce 2D monolayer alloys is to synthesize bulk crystal alloys and obtain monolayer samples by mechanical exfoliation. For example, $Mo_xW_{1-x}Se_2$ bulk crystals were synthesized across the full range of compositions, and mechanical exfoliation was performed to produce alloy monolayers[49]. The bandgap dependence on the composition in these monolayer alloys was examined by several methods; strong PL emission peaks in the range 1.56–1.65 eV indicated a direct bandgap for the entire range of compositions.

Abrupt heterojunctions and heterostructures made of 2D monolayers have attracted considerable interest over the past 2–3 years. Most heterostructures involve a change of the transition metal element between Mo and W (REFS 50–55) across the interface, whereas the common element is either S or Se. Nevertheless, heterostructures in which chalcogen elements are switched between S and Se and the shared transition metal element is either Mo or W (REF. 55) have also been created. There have also

been studies of heterostructures in which both the transition metal and chalcogen elements were switched at the interface, as in the case of MoS_2/WSe_2, demonstrating an excellent control of the interface, which was atomically sharp[56]. This research is still in the early stages, mostly focusing on the creation of the heterostructures, similar to the early days of heterostructure studies involving traditional III–V or II–VI semiconductors. Charge and field control remain considerable challenges, as do the injection and confinement of carriers. These are key issues for the realization of practical devices with current or voltage control, especially optoelectronic devices.

Halide perovskite alloy nanomaterials

Structure and properties of halide perovskites. Perovskites are a large family of compounds described by the general formula ABX_3, consisting of corner-sharing BX_6 octahedra with a 12-fold coordinated A cation occupying the site in the middle of the cube defined by eight octahedra[57]. Recently, there has been a renaissance of halide perovskites (with A = organic ammonium cation or Cs^+; B = Pb^{2+}; X = Cl^-, Br^- or I^-), which are a class of semiconductor materials holding promise for many applications[58–60]. Remarkable features have been discovered in halide perovskite systems, including strong optical absorption, long charge carrier lifetime and/or diffusion length, high photoluminescence quantum yield (PLQY) and low-temperature solution processability. Highly efficient thin-film optoelectronic devices such as photovoltaic and light-emitting devices and photodetectors based on these materials have been demonstrated[61–63]. Meanwhile, the chemical management of the compositional elements has proved to be an effective method to refine the properties of halide perovskites.

Very recently, novel halide perovskite nanostructures, including 0D quantum dots, 1D nanowires and 2D quantum wells, have been synthesized using both solution-based and vapour deposition methods[64]. Alloying provides an extra degree of freedom for the continuous tuning of the optical and electronic properties of perovskites without changing the particle size and morphology, and can potentially induce composition-dependent properties in addition to the quantum confinement effect. For example, alloying with cations or anions can lead to the phase stabilization of metastable iodide perovskites[65–67]. Owing to the dynamic nature of the halide perovskite lattice, alloying can be achieved both by direct one-pot synthesis and by post-synthetic methods, such as ion-exchange reactions. These ionic semiconducting nanomaterials with excellent optical and electronic properties provide a versatile platform for understanding alloy and heterostructure formation, as well as for applications in optoelectronics[31,68,69].

Direct synthesis. Alloyed perovskite nanostructures have been prepared through direct synthetic methods including colloidal synthesis, solution-phase recrystallization processes and vapour-phase approaches. The colloidal synthesis of halide perovskite $CsPbX_3$ (X = Cl, Br or I) quantum dots (QDs) was achieved[70] by the controlled precipitation of Cs^+, Pb^{2+} and X^- ions into $CsPbX_3$ by rapid injection of caesium oleate into a hot solution of PbX_2 (FIG. 5a). The mixed-halide perovskites $CsPb(Cl/Br)_3$ and $CsPb(Br/I)_3$ could be readily produced by varying the molar ratio of PbX_2 precursors (the Cl/I alloy could not be obtained owing to the large lattice mismatch). The alloyed nanocrystals showed bright PL, which could be tuned over the entire visible region (FIG. 5b). As for CdSe QDs, size-dependent PL emission (due to quantum confinement) was observed in halide perovskite QDs. For example, $CsPbBr_3$ QDs with sizes of 3.8 nm and 11.8 nm exhibit emission peaks at ~470 nm (~2.64 eV) and ~515 nm (~2.41 eV), respectively. For $CsPbBr_3$, the effective Bohr diameter of Wannier–Mott excitons and the binding energy were estimated to be ~7 nm and 40 meV, respectively. The QD suspensions showed long carrier lifetimes, ranging from 1 to 29 ns (FIG. 5c). The more iodide present, the longer the lifetime, which is consistent with the trend in bulk thin films[59]. The initial success of this method motivated more research in this direction. By extending the reaction duration and replacing oleic acid with octylamine for the PbX_2 precursor[71], it was possible to obtain $CsPbBr_3$ nanowires with a diameter of ~10 nm and an average length of more than 10 μm. Lowering the reaction temperature to ~80 °C led to the formation of 2D nanosheets with diameters of ~100 nm and thicknesses of a few unit cells[72]. In another work[73], caesium oleate was dissolved in oleic acid instead of octadecene, which improved the lateral size of the 2D sheets to ~1 μm. It was also shown that the choice of protecting ligands has an important role in determining the morphology of the nanocrystals[74]. All these experiments indicate that the colloidal reaction is highly dynamic and the nanoscale morphology continues evolving during the reaction. Using the colloidal method, other related materials, such as $MAPbX_3$ (MA = methylammonium) and $CsSnX_3$ have been synthesized and studied in detail[75–77].

The strongly ionic and relatively weak bonding in halide perovskites makes them soluble in certain polar organic solvents. This enables direct crystallization of halide perovskites from such polar organic solvents. To gain better control over the nanoscale morphology, a substrate can be introduced to guide the nanocrystal growth. Recent experiments have shown that high-quality $MAPbX_3$ and $CsPbX_3$ nanowires (a few hundreds of nanometres in diameter) and thin plates (a few hundreds of nanometres thick) with rectangular cross sections and well-defined end facets can be grown using the substrate-guided method[31,78]. For example, nanowires, including $CsPbBr_3$ nanowires (FIG. 5d), were grown by spin-casting a thin layer of PbX_2 on a piece of glass (sometimes coated with poly(3,4-ethylenedioxythiophene) polystyrene sulfonate, PEDOT:PSS) for wetting purposes), after which the whole substrate was immersed in a solution containing MAX or CsX precursors. It is believed that Pb can slightly dissolve into the solution and recrystallize on the substrate, leading to the formation of ideal perovskite structures. Also in this case, the composition and bandgap of the nanowires and plates could be tuned simply by blending different anion precursors during the growth. The X-ray diffraction peaks (110) and (002) gradually shifted as the nanowire composition was changed from pure $CsPbBr_3$ to pure $CsPbCl_3$

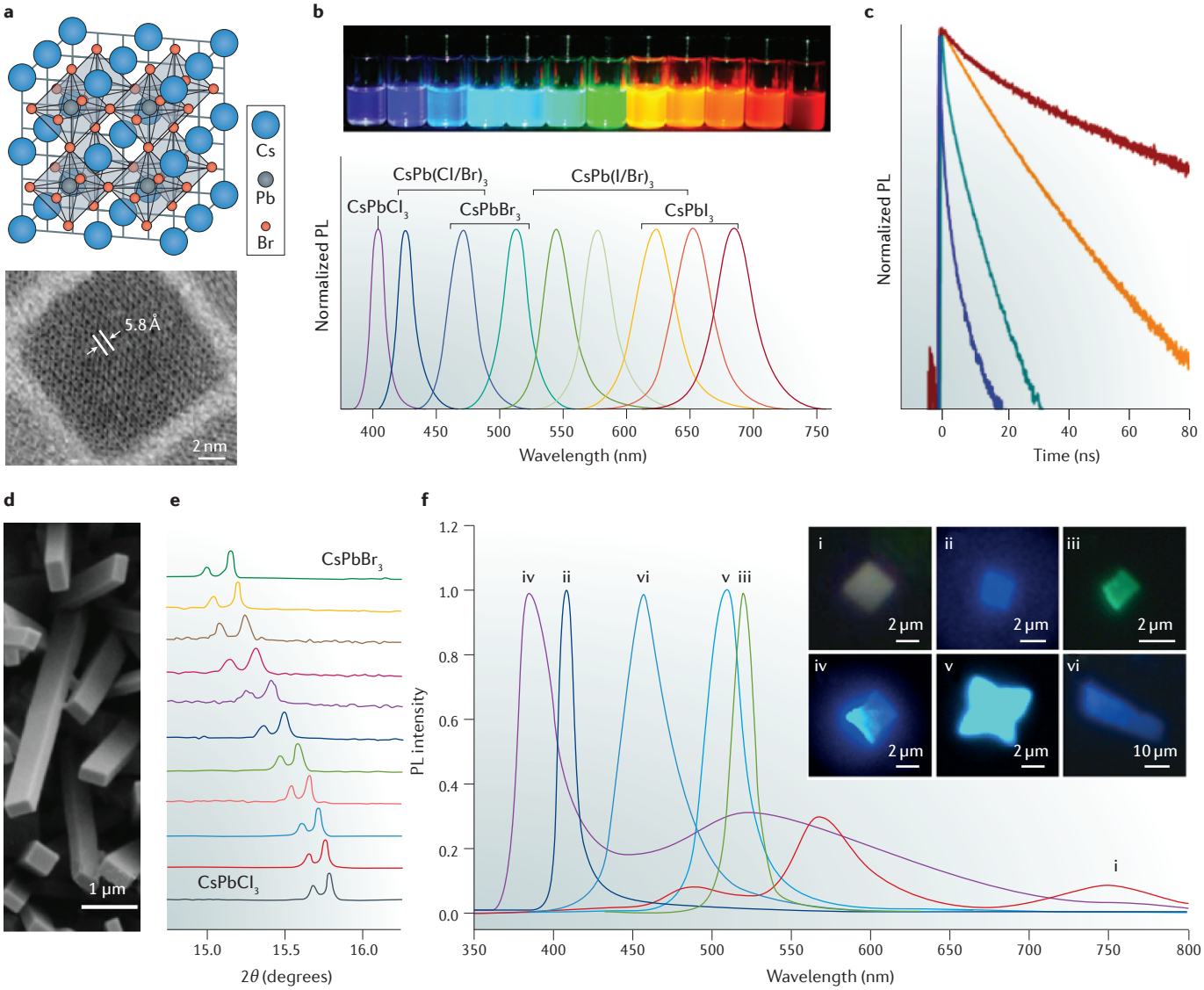

Figure 5 | **Direct synthesis of halide perovskite alloy nanomaterials. a** | Crystal structure of $CsPbBr_3$ accompanied by a high-resolution transmission electron microscopy image of a typical $CsPbBr_3$ nanocrystal with a lateral size of ~8 nm. **b** | Colloidal solutions of $CsPbX_3$ (X = Cl, Br or I) nanocrystals and alloys with different compositions and particle sizes in toluene under a UV lamp (λ = 365 nm) and their photoluminescence (PL) spectra. **c** | Time-resolved PL decays for representative samples from panel **b** showing the charge carrier lifetimes. **d** | Scanning electron microscopy image of as-grown $CsPbBr_3$ nanowires showing flat-end facets and rectangular cross sections with various width-to-thickness ratios. **e** | Spectra showing the shift of the X-ray diffraction peaks observed as the composition of the nanowires is changed from pure $CsPbBr_3$ to pure $CsPbCl_3$. **f** | PL spectra and corresponding optical PL images for different 2D perovskite crystals: (i) $(C_4H_9NH_3)_2PbCl_4$; (ii) $(C_4H_9NH_3)_2PbBr_4$; (iii) $(C_4H_9NH_3)_2PbI_4$; (iv) $(C_4H_9NH_3)_2PbCl_2Br_2$; (v) $(C_4H_9NH_3)_2PbBr_2I_2$; and (vi) $(C_4H_9NH_3)_2(CH_3NH_3)Pb_2Br_7$. Panels **a**–**c** are adapted with permission from REF. 70, American Chemical Society. Panels **d** and **e** are adapted with permission from REF. 79, American Chemical Society. Panel **f** is adapted with permission from REF. 86, AAAS.

through alloying (FIG. 5e). Colour-tunable nanowire lasers were achieved using these high-quality perovskite alloys[79]. Note that nanowires and 2D plates with similar dimensions can also be synthesized using vapour deposition methods[80–84].

The growth of 2D halide perovskites with one or few perovskite metal–halide layers represents another challenge in nanomaterials chemistry. The substrate-recrystallization and vapour deposition methods usually give nanowires and 2D plates with a size of several hundreds of nanometres. By contrast, colloidal synthesis only produces ultrathin 2D sheets with relatively small diameters[85]. To achieve atomically thin 2D perovskites, a substrate-guided method involving solvent evaporation was developed[86]. A layered perovskite, $(C_4H_9NH_3)_2PbX_4$, was used as the model material. A very dilute precursor solution was dropped on a flat substrate (for example SiO_2/Si) and then dried under mild heating. A

ternary dimethylformamide–chlorobenzene–acetonitrile co-solvent was used because chlorobenzene and acetonitrile help to reduce the solubility of precursors in dimethylformamide and promote crystallization. Several 2D sheets and alloys, including $(C_4H_9NH_3)_2PbCl_4$, $(C_4H_9NH_3)_2PbI_4$, $(C_4H_9NH_3)_2PbCl_2Br_2$, $(C_4H_9NH_3)_2PbBr_2I_2$ and $(C_4H_9NH_3)_2(CH_3NH_3)Pb_2Br_7$, were successfully prepared and optically characterized (FIG. 5f). A better understanding of the underlying growth mechanism in this method still needs to be acquired. A recent work investigated the influence of some key factors, including the solvent/volume ratio, crystallization temperature and solvent polarity, on the growth dynamics of the 2D sheets[87].

Halide perovskite alloys and heterostructures grown through ion exchange. The use of ion exchange to synthesize bulk materials is limited by the sluggish ion diffusion kinetics over large length scales. By contrast, it works well for nanomaterials owing to the short distance ions need to travel. In recent years, ion exchange has been used to synthesize a variety of nanomaterials, nanoscale heterostructures and alloys. A key feature of halide perovskite semiconductors is the highly dynamic crystal lattice. This promotes facile ion migration so that halide perovskites can easily exchange their ions with other ions from the surrounding environment. Starting from $CsPbBr_3$ QDs, fast anion exchange with its iodide and chloride counterparts was demonstrated[88]. The anion-exchange reaction happens at the solid/liquid interface. Both organic and inorganic halide precursors can be used, and the exchange reaction happens at room temperature or under mild heating (<90 °C) on a timescale from a few seconds to a few minutes (FIG. 6a). The optical bandgap can be tuned from 1.8 to 3.0 eV by varying the ratio of different halides (FIG. 6b); the QD alloys retain good crystallinity and high PLQY after the anion-exchange reaction, similar to those of the directly synthesized QDs (FIG. 6c). In *in situ* PL studies, the presence of two distinct exchange mechanisms during anion exchange in $CsPbX_3$ QDs was established[89]. It was found that the Br–I exchange is a surface-reaction-limited mechanism allowing for rapid alloying, whereas the Br–Cl exchange is a diffusion-limited exchange process resulting in the formation of zones of exchange. The exchange strategy was then extended to 1D nanowires without damage to the surface morphology and optical properties of the ultrathin and long wires[71] (FIG. 6d). Anion exchange can also happen at solid/gas interfaces under vapour treatment[79]. Organic ammonium halides with low molecular weights are normally used (such as methylammonium halides or butylammonium halides) because they slightly evaporate (decomposing to amine and hydrogen halides) under mild heating (~100 °C). The halide species in the vapour react with the perovskites, replacing the original halides. The exact exchange mechanism is still under investigation.

It was recently shown that the B-site cation can also be partially exchanged using the colloidal method to realize alloys with mixed cations[90]. Using $CsPbBr_3$ QDs, Pb^{2+} was exchanged for several isovalent cations, leading to doped $CsPb_{1-x}M_xBr_3$ QDs ($M^{2+} = Sn^{2+}$, Cd^{2+} and Zn^{2+}; $0 < x \leq 0.1$), with excellent preservation of the original QD shape. The partial exchange of Pb^{2+} for M^{2+} led to a blue shift in the PL emission spectra while maintaining the high PLQY (>50%), sharp absorption features and narrow emission. The blue shift in the optical spectra was attributed to the lattice contraction upon the introduction of smaller cations (FIG. 6e).

The soft nature of halide perovskites enables the formation of uniform alloys with a wide range of compositions and tunable properties without the need to worry excessively about lattice mismatches (note that the lattice mismatch between different perovskite phases of $MAPbX_3$ and $CsPbX_3$ that are stable at room temperature ranges from 3 to 10%, which is quite large). However, there could be stability-related issues. Evidence of phase segregation in perovskite alloys under strong optical excitation has been reported in the bromide–iodide system, and theory suggests that spinodal decomposition to purer phases may occurr[91]. Acquiring precise control of the manipulation of the ions inside the halide perovskite alloys is the next challenge. To this end, composition-graded nanostructures and heterojunctions inside a nanostructure domain will be of great interest for fundamental understanding of the charge carrier and ion dynamics and for applications in nanoscale optoelectronics[92].

Applications

In the introduction, we discussed in general terms how various photonic applications can benefit from a wide range of bandgaps. Certain unique applications have also been mentioned while reviewing specific materials. Here, we highlight a few important applications that are (or could be) enabled by nanomaterials with bandgap flexibility or tunability.

New solar cells. Nanowire-based tandem multijunction solar cells could benefit from bandgap optimization to improve efficiency, or more bandgaps (junctions) could be realized by taking advantage of the large tolerance to lattice mismatches. However, owing to the need for tunnel junctions in tandem designs, such nanowire-based solar cells will be challenging to realize in the near future. By contrast, multiple lateral junction designs for dispersive concentration photovoltaics (DCPV) are more promising. The DCPV concept has existed for several decades. The main challenge has been the production of the required cells in a cost-efficient manner. Multibandgap nanomaterials can be grown in a single step on a single substrate to produce all the bandgaps needed to form laterally arranged multiple-bandgap cells in a true low-cost fashion[93–95]. The high quality of the nanowires and the associated photon management or light trapping can lead to good efficiencies. Thus, in the long term, this is a true low-cost and high-efficiency approach. The design[93] and proof-of-concept devices[94,95] have been realized, but more research is needed to demonstrate their true potential for high efficiency.

Widely tunable semiconductor lasers. Tunable semiconductor lasers are important for many applications, including telecommunications, biological and chemical detectors, colour displays and lighting. However,

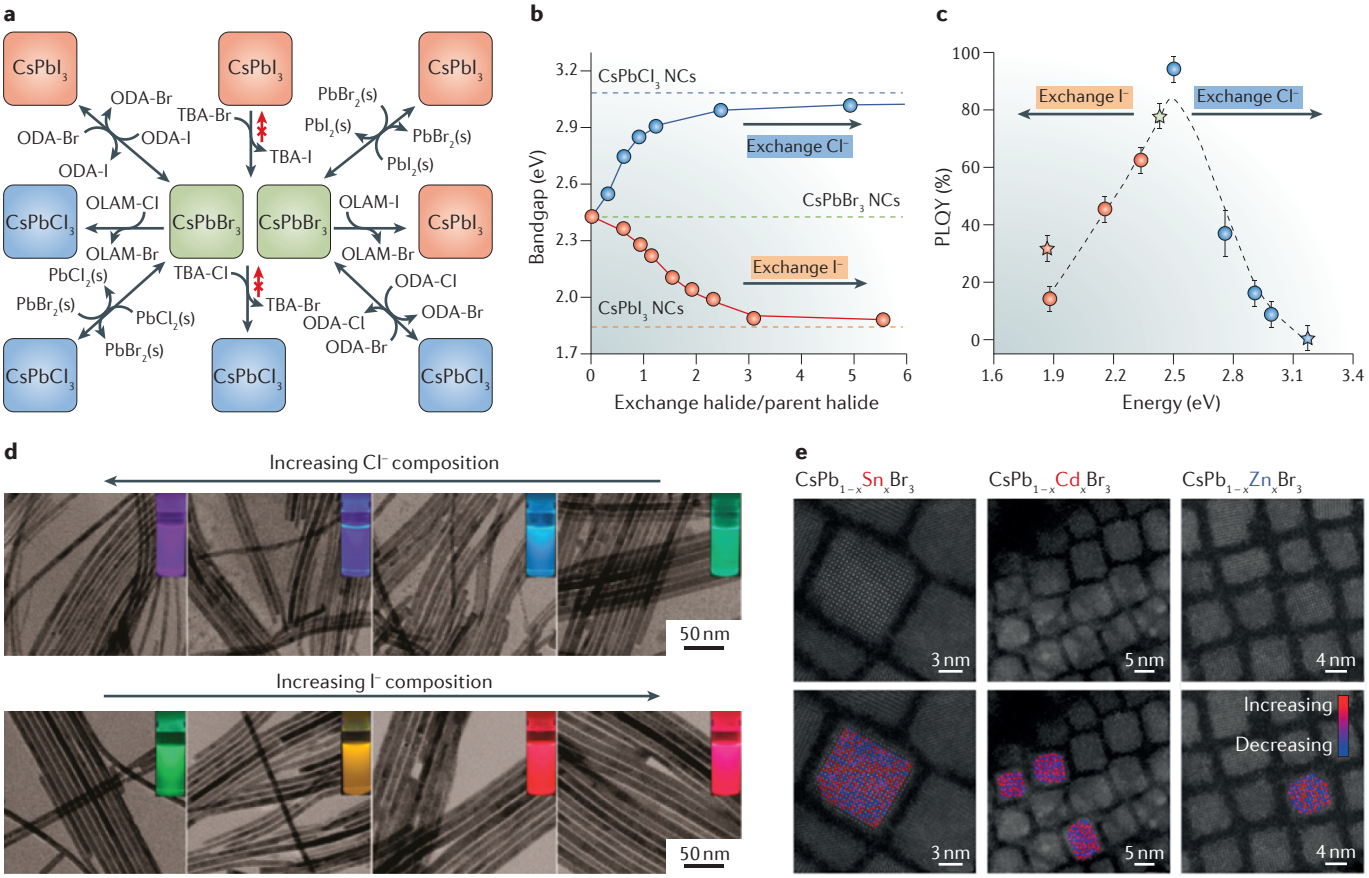

Figure 6 | **Halide perovskite alloys grown through ion exchange. a** | Overview of the different routes and precursors for the anion-exchange reactions of $CsPbBr_3$ quantum dots (QDs). **b** | Photoluminescence (PL) calibration curves showing that a targeted emission energy can be obtained by adding a precise amount of halide precursor to a crude solution of $CsPbBr_3$ QDs. The curves are reported as a function of the molar ratio between the added halide (or exchange halide) and the amount of Br^- in the starting QDs. **c** | Photoluminescence quantum yield (PLQY) recorded on the exchanged QDs (circles) and on the directly synthesized QDs (stars). **d** | Transmission electron microscopy (TEM) images of $CsPbX_3$ nanowires with various degrees of conversion with Cl^- (top row) and I^- (bottom row). The insets show the evolution of the emission colour (UV excitation, $\lambda = 365$ nm) upon the formation of mixed-halide alloy nanowires. **e** | Quantitative high-angle annular dark-field scanning TEM images reveal a lattice contraction of the parent $CsPbBr_3$ QDs ($|a| = 5.849 \pm 0.003$ Å) upon alloying with Sn^{2+} ($|a| = 5.839 \pm 0.005$ Å), Cd^{2+} ($|a| = 5.819 \pm 0.008$ Å) and Zn^{2+} ($|a| = 5.808 \pm 0.014$ Å); $|a|$ is the lattice constant of the unit cell. The top panels show that the mixed Pb–halide (bright contrast), Cs^{2+} (intermediate contrast) and halide (low contrast) atomic columns can be easily assigned. The bottom panels show the interatomic distances calculated after detecting the positions of the Pb–halide columns. Red and blue bars indicate larger and smaller distances than the mean $|a|$, respectively. NC, nanocrystal; ODA, octadecylammonium; OLAM, oleylammonium; TBA, tetrabutylammonium. Panels **a**–**c** are adapted with permission from REF. 88, American Chemical Society. Panel **d** is adapted with permission from REF. 71, American Chemical Society. Panel **e** is adapted with permission from REF. 90, American Chemical Society.

semiconductor tunable lasers are limited by the gain bandwidth of a single semiconductor. As discussed, spatially tunable lasers grown on a single substrate, lasing with multiple wavelengths from a single nanowire or nanosheet, and white lasers have been demonstrated. They all represent important steps forward compared with what can be realized using traditional planar epitaxial growth. For a more general discussion of nanowire-based lasers, we refer the reader to recent review articles[96–99].

Semiconductor displays, illumination and lighting. Displays and lighting require the ability to generate light inexpensively and in the complete range of visible colours. Nanoscale semiconductor materials such as nanowires and nanosheets provide the opportunity to produce light sources by means of all-inorganic semiconductors, possibly in a monolithic form, greatly reducing the cost, improving the efficiency and prolonging the lifetime of such devices. In the future, it may even be possible to use multicolour, full-colour or white lasers in all these applications, further improving efficiency and brightness.

Artificial photosynthesis. Artificial photosynthesis aims at mimicking the natural photosynthesis process to convert and store solar energy in chemical form. In the photochemical diode design[100,101], which enables the absorption of multiple solar emission bands, various

processes need to be optimized, including solar absorption, band alignment and current balance between photoelectrodes, electrochemical reactions during electrolysis and overall system performance and balance. Depending on the specific chemical reactions driven by the photocarriers, different bandgaps are required, often distinct from those provided by available compounds. Semiconductor alloying in nanomaterials provides flexibility for both the required bandgaps and the p–n junction alignment.

Conclusions and perspectives

In this Review, we focused on the important emerging theme of bandgap engineering through alloying with control over a wide range of compositions that is enabled by nanoscale materials and summarized the most important progress made over the past decade. As the field is still young and evolving, many issues remain to be studied. These include strain and mismatch during growth and their effect on the quality of the material, the uniformity of alloying in different dimensionalities and its effect on carrier mobilities. The progress has been impressive, but so are the remaining challenges.

Electrical injection devices. One of the greatest advantages of semiconductor-based lasers and light-emitting devices is the ability to inject carriers electrically by applying a bias. The electrical injection is crucial for the ease of use, efficiency and integration in compact platforms for various applications. However, many of the unique devices that we have discussed, such as multicolour or white lasers, are currently optically pumped. It is now time to focus on electrical injection devices. There are some obvious challenges for electrical injection. First of all, an efficient injection configuration is essential. There have been studies of electrical injection into nanowire devices with longitudinal or radial p–n or p–i–n structures[102,103], with the latter being the most efficient injection scheme. However, the growth of a radial p–i–n structure with sufficiently high injection levels and adequately large gain regions remains challenging. Controllable doping, including the doping level and spatial profile, is also an issue. Instead of individual nanowires, arrays of nanowires with thin-film injection and contact layers seem to be a near-term compromise. Although this solution will not help to produce individual nanowire lasers with small footprints, it creates new opportunities for fabricating lasers with wavelengths that are often inaccessible using planar growth technologies. More than 10 years after the first electrical-injection individual nanowire lasers[104], this remains a difficult task. Monolithic RGB nanosheet structures could enable multicolour or white LEDs for displays and lighting. However, new device designs are needed to achieve such LED operation with electrical injection.

Alignment of nanowires. As we emphasized in the introduction, the small cross section and large tolerance to lattice mismatches help to grow materials with a wide array of compositions and bandgaps on a single substrate. However, different levels of strain affect the growth process and the resulting nanowires differently. Such effects have not been studied systematically, although they are important for the optimization of the growth conditions for obtaining nanowires with controlled orientation. Most of the experiments on the synthesis of composition-graded and bandgap-graded materials produced nanowires and other nanostructures with random orientations. Such samples are adequate for studying the material properties based on pick-and-place transfer methods, but in the long term, to achieve more controlled device fabrication, a strategy to fabricate nanowire arrays has to be developed. For variations in composition that are too large for a given substrate, simple epitaxial growth is not sufficient. Templates such as those based on anodic aluminium oxide (AAO) pores[105] could be useful, but the standard AAO pores are too small for many nanowire device applications or for VLS growth. Other pore template techniques have to be developed to address the growth of materials with very large lattice mismatches.

Concluding remarks. In summary, nanotechnology is at a critical transition stage, moving from materials science to device development. Innovative device designs and fabrication techniques are needed to enable a successful transition. Semiconductor alloy nanomaterials with widely varying compositions set new challenges for materials growth and control, as well as for device fabrication. In addition, these materials provide new opportunities for ultimate bandgap engineering at the nanoscale and for new applications.

1. Glas, F. Critical dimensions for the plastic relaxation of strained axial heterostructures in free-standing nanowires. *Phys. Rev. B* **74**, 121302 (2016).
2. Martensson, T. *et al.* Epitaxial growth of indium arsenide nanowires on silicon using nucleation templates formed by self-assembled organic coatings. *Adv. Mater.* **19**, 1801–1806 (2007).
3. Tomioka, K. *et al.* Control of InAs nanowire growth directions on Si. *Nano Lett.* **8**, 3475–3480 (2008).
4. Bjork, M. T. *et al.* One-dimensional steeplechase for electrons realized. *Nano Lett.* **2**, 87–89 (2002).
5. Assali, S. *et al.* Direct band gap wurtzite gallium phosphide nanowires. *Nano Lett.* **13**, 1559–1563 (2013).
6. Yuan, X. *et al.* Controlling the morphology, composition and crystal structure in gold-seeded $GaAs_{1-x}Sb_x$ nanowires. *Nanoscale* **7**, 4995–5003 (2015).
7. Martensson, A. T. *et al.* Epitaxial III-V nanowires on silicon. *Nano Lett.* **4**, 1987–1990 (2004).
8. Tomioka, K., Yoshimura, M. & Fukui, T. A III–V nanowire channel on silicon for high-performance vertical transistors. *Nature* **488**, 189–192 (2012).
9. Borg, M. *et al.* Vertical III–V nanowire device integration on Si(100). *Nano Lett.* **14**, 1914–1920 (2014).
10. Cohin, Y. *et al.* Growth of vertical GaAs nanowires on an amorphous substrate via a fiber-textured Si platform. *Nano Lett.* **13**, 2743–2747 (2013).
11. Mayer, B. *et al.* Monolithically integrated high-β nanowire lasers on silicon. *Nano Lett.* **16**, 152–156 (2016).
12. Schuster, F. *et al.* Site-controlled growth of monolithic InGaAs/InP quantum well nanopillar lasers on silicon. *Nano Lett.* **17**, 2697–2702 (2017).
13. Kim, H. *et al.* Monolithically integrated InGaAs nanowires on 3D structured silicon-on-insulator as a new platform for full optical links. *Nano Lett.* **16**, 1833–1839 (2016).
14. Nguyen, H. T. *et al.* p-Type modulation doped InGaN/GaN dot-in-a-wire white-light-emitting diodes monolithically grown on Si(111). *Nano Lett.* **11**, 1919–1924 (2011).
15. Chen, R. *et al.* Nanolasers grown on silicon. *Nat. Photonics* **5**, 170–175 (2011).
16. Ihn, S. G. *et al.* Morphology- and orientation-controlled gallium arsenide nanowires on silicon substrates. *Nano Lett.* **7**, 39–44 (2007).
17. Hazari, A., Aiello, A., Ng, T. K., Ooi, B. S. & Bhattacharya, P. III-nitride disk-in-nanowire 1.2 μm monolithic diode laser on (001) silicon. *Appl. Phys. Lett.* **107**, 191107 (2015).
18. Deshpande, S. *et al.* Formation and nature of InGaN quantum dots in GaN nanowires. *Nano Lett.* **15**, 1647–1653 (2015).
19. Qian, Y. *et al.* Multi-quantum-well nanowire heterostructures for wavelength-controlled lasers. *Nat. Mater.* **7**, 701–706 (2008).

20. Bhattacharya, P., Hazari, A., Jahangir, S., Guo, W. & Frost, T. III-Nitride electrically pumped visible and near-infrared nanowire lasers on (001) silicon. *Semicond. Semimetals* **96**, 385–409 (2017).
21. Gwo, S. *et al.* Nitride semiconductor nanorod heterostructures for full-color and white-light applications. *Semicond. Semimetals* **96**, 341–384 (2017).
22. Zhao, S. & Mi, Z. Al(Ga)N nanowire deep ultraviolet optoelectronics. *Semicond. Semimetals* **96**, 167–199 (2017).
23. Berg, A. *et al.* Growth and optical properties of $In_xGa_{1-x}P$ nanowires synthesized by selective-area epitaxy. *Nano Res.* **10**, 672–682 (2017).
24. Tomioka, K. & Fukui, T. in *Semiconductor Nanostructures for Optoelectronic Devices* (ed. Yi, G.-C.) 67–101 (Springer, 2012).
25. Jacobsson, D. *et al.* Particle-assisted $Ga_xIn_{1-x}P$ nanowire growth for designed bandgap structures. *Nanotechnology* **23**, 245601–245607 (2012).
26. Gagliano, L. *et al.* Pseudodirect to direct compositional crossover in wurtzite GaP/$In_xGa_{1-x}P$ core–shell nanowires. *Nano Lett.* **16**, 7930–7936 (2016).
27. Kornienko, N. *et al.* Solution phase synthesis of indium gallium phosphide alloy nanowires. *ACS Nano* **9**, 3951–3960 (2015).
28. Amiri, S. E. H., Ranga, P., Li, D. Y., Fan, F. & Ning, C. -Z. Growth of InGaP alloy nanowires with widely tunable bandgaps on silicon substrates. *CLEO Sci. Innov.* http://dx.doi.org/10.1364/CLEO_SI.2017.STh3I.4 (2017).
29. Zhuang, X. Ning, C. Z. & Pan, A. Composition and bandgap-graded semiconductor alloy nanowires. *Adv. Mater.* **24**, 13–33 (2012).
30. Nichols, P. L. *et al.* $Cd_xPb_{1-x}S$ alloy nanowires and heterostructures with simultaneous emission in mid-infrared and visible wavelengths. *Nano Lett.* **15**, 909–916 (2015).
31. Zhu, H. *et al.* Lead halide perovskite nanowire lasers with low lasing thresholds and high quality factors. *Nat. Mater.* **14**, 637–642 (2015).
32. Pan, A., Liu, R., Sun, M. & Ning, C. Z. Quaternary alloy semiconductor nanobelts with bandgap spanning the entire visible spectrum. *J. Am. Chem. Soc.* **131**, 9502–9503 (2009).
33. Kuykendall, T. *et al.* Complete composition tunability of InGaN nanowires using a combinatorial approach. *Nat. Mater.* **6**, 951–956 (2007).
34. Liu, Y. *et al.* Wavelength-controlled lasing in $Zn_xCd_{1-x}S$ single crystal nanoribbons. *Adv. Mater.* **17**, 1372–1377 (2005).
35. Pan, A. *et al.* Color-tunable photoluminescence of alloyed CdS_xSe_{1-x} nanobelts. *J. Am. Chem. Soc.* **127**, 15692–15693 (2005).
36. Pan, A. *et al.* Continuous alloy-composition spatial grading and superbroad wavelength-tunable nanowire lasers on a single chip. *Nano Lett.* **9**, 784–788 (2009).
37. Pan, A., Liu, R., Sun, M. & Ning, C. Z. Spatial composition grading of quaternary ZnCdSSe alloy nanowires with tunable light emission between 350 and 710 nm on a single substrate. *ACS Nano* **4**, 671–680 (2010).
38. Yang, Z. Y. *et al.* On-nanowire spatial band gap design for white light emission. *Nano Lett.* **11**, 5085–5089 (2011).
39. Yang, Z. *et al.* Broadly defining lasing wavelengths in single bandgap-graded semiconductor nanowires. *Nano Lett.* **14**, 3153–3159 (2014).
40. Liu, Z. *et al.* Dynamical color-controllable lasing with extremely wide tuning range from red to green in a single alloy nanowire using nanoscale manipulation. *Nano Lett.* **13**, 4945–4950 (2013).
41. Fan, F. *et al.* Simultaneous two-color lasing in a single CdSSe heterostructure nanosheet. *Semicond. Sci. Technol.* **28**, 065005 (2013).
42. Fan, F. *et al.* A monolithic white laser. *Nat. Nanotechnol.* **10**, 796–803 (2015).
43. Turkdogan, S., Fan, F. & Ning, C. Z. Color-temperature tuning and control of trichromatic white light emission from a multisegment ZnCdSSe heterostructure nanosheet. *Adv. Funct. Mater.* **26**, 8521–8526 (2016).
44. Kang, J., Tongay, S., Zhou, J., Li, J. & Wu, J. Band offsets and heterostructures of two-dimensional semiconductors. *Appl. Phys. Lett.* **102**, 012111–012114 (2013).
45. Xie, L. M. Two-dimensional transition metal dichalcogenide alloys: preparation, characterization and applications. *Nanoscale* **7**, 18392–18401 (2015).
46. Feng, Q. *et al.* Growth of large-area 2D $MoS_{2(1-x)}Se_{2x}$ semiconductor alloys. *Adv. Mater.* **26**, 2648–2653 (2014).
47. Feng, Q. *et al.* Growth of $MoS_{2(1-x)}Se_{2x}$ (x = 0.41–1.00) monolayer alloys with controlled morphology by physical vapor deposition. *ACS Nano* **9**, 7450–7455 (2015).
48. Su, S. *et al.* Band gap-tunable molybdenum sulfide selenide monolayer alloy. *Small* **10**, 2589–2594 (2014).
49. Zhang, M. *et al.* Two-dimensional molybdenum tungsten diselenide alloys: photoluminescence, Raman scattering, and electrical transport. *ACS Nano* **8**, 7130–7137 (2014).
50. Gong, Y. *et al.* Vertical and in-plane heterostructures from WS_2/MoS_2 monolayers. *Nat. Mater.* **13**, 1135–1142 (2014).
51. Hong, X. *et al.* Ultrafast charge transfer in atomically thin MoS_2/WS_2 heterostructures. *Nat. Nanotechnol.* **9**, 682–686 (2014).
52. Li, M. Y. *et al.* Epitaxial growth of a monolayer WSe_2-MoS_2 lateral p-n junction with an atomically sharp interface. *Science* **349**, 524–528 (2015).
53. Gong, Y. *et al.* Two-step growth of two-dimensional WSe_2/$MoSe_2$ heterostructures. *Nano Lett.* **15**, 6135–6141(2015).
54. Huang, C. *et al.* Lateral heterojunctions within monolayer $MoSe_2$-WSe_2 semiconductors. *Nat. Mater.* **13**, 1096–1101 (2014).
55. Duan, X. *et al.* Lateral epitaxial growth of two-dimensional layered semiconductor heterojunctions. *Nat. Nanotechnol.* **9**, 1024–1030 (2014).
56. Cheng, R. *et al.* Electroluminescence and photocurrent generation from atomically sharp WSe_2/MoS_2 heterojunction p–n diodes. *Nano Lett.* **14**, 5590–5597 (2014).
57. Peña, M. A. & Fierro, J. L. G. Chemical structures and performance of perovskite oxides. *Chem. Rev.* **101**, 1981–2018 (2001).
58. Green, M. A., Ho-Baillie, A. & Snaith, H. J. The emergence of perovskite solar cells. *Nat. Photonics* **8**, 506–514 (2014).
59. Manser, J. S., Christians, J. A. & Kamat, P. V. Intriguing optoelectronic properties of metal halide perovskites. *Chem. Rev.* **116**, 12956–13008 (2016).
60. Li, W. *et al.* Chemically diverse and multifunctional hybrid organic–inorganic perovskites. *Nat. Rev. Mater.* **2**, 16099 (2017).
61. Zhou, H. *et al.* Interface engineering of highly efficient perovskite solar cells. *Science* **345**, 542–546 (2014).
62. Tan, Z.-K. *et al.* Bright light-emitting diodes based on organometal halide perovskite. *Nat. Nanotechnol.* **9**, 687–692 (2014).
63. Dou, L. *et al.* Solution-processed hybrid perovskite photodetectors with high detectivity. *Nat. Commun.* **5**, 5404 (2014).
64. Ha, S.-T., Su, R., Xing, J., Zhang, Q. & Xiong, Q. Metal halide perovskite nanomaterials: synthesis and applications. *Chem. Sci.* **8**, 2522–2536 (2017).
65. Protesescu, L. *et al.* Dismantling the "red wall" of colloidal perovskites: highly luminescent formamidinium and formamidinium – cesium lead iodide nanocrystals. *ACS Nano* **11**, 3119–3134 (2017).
66. Fu, Y. *et al.* Nanowire lasers of formamidinium lead halide perovskites and their stabilized alloys with improved stability. *Nano Lett.* **16**, 1000–1008 (2016).
67. Piatkowski, P. *et al.* Unraveling charge carriers generation, diffusion, and recombination in formamidinium lead triiodide perovskite polycrystalline thin film. *J. Phys. Chem. Lett.* **7**, 204–210 (2016).
68. Sutherland, B. R. & Sargent, E. H. Perovskite photonic sources. *Nat. Photonics* **10**, 295–302 (2016).
69. Swarnkar, A. *et al.* Quantum dot–induced phase stabilization of α-$CsPbI_3$ perovskite for high-efficiency photovoltaics. *Science* **354**, 92–95 (2016).
70. Protesescu, L. *et al.* Nanocrystals of cesium lead halide perovskites ($CsPbX_3$, X = Cl, Br, and I): novel optoelectronic materials showing bright emission with wide color gamut. *Nano Lett.* **15**, 3692–3696 (2015).
71. Zhang, D. *et al.* Synthesis of composition tunable and highly luminescent cesium lead halide nanowires through anion-exchange reactions. *J. Am. Chem. Soc.* **238**, 7236–7239 (2016).
72. Bekenstein, Y. Koscher, B. A., Eaton, S. W., Yang, P. & Alivisatos, A. P. Highly luminescent colloidal nanoplates of perovskite cesium lead halide & their oriented assemblies. *J. Am. Chem. Soc.* **137**, 16008–16011 (2015).
73. Shamsi, J. *et al.* Colloidal synthesis of quantum confined single crystal $CsPbBr_3$ nanosheets with lateral size control up to the micrometer range. *J. Am. Chem. Soc.* **138**, 7240–7243 (2016).
74. Pan, A. *et al.* Insight into the ligand-mediated synthesis of colloidal $CsPbBr_3$ perovskite nanocrystals: the role of organic acid, base, and cesium precursors. *ACS Nano* **10**, 7943–7954 (2016).
75. Schmidt, L. C. *et al.* Nontemplate synthesis of $CH_3NH_3PbBr_3$ perovskite nanoparticles. *J. Am. Chem. Soc.* **136**, 850–853 (2014).
76. Zhao, Y., Xu, X. & You, X. Colloidal organometal halide perovskite ($MAPbBr_xI_{3-x}$, $0 \le x \le 3$) quantum dots: controllable synthesis and tunable photoluminescence. *Sci. Rep.* **6**, 35931 (2016).
77. Jellicoe, T. *et al.* Synthesis and optical properties of lead-free cesium tin halide perovskite nanocrystals. *J. Am. Chem. Soc.* **138**, 2941–2944 (2016).
78. Eaton, S. W. *et al.* Lasing in robust cesium lead halide perovskite nanowires. *Proc. Natl Acad. Sci. USA* **113**, 1993–1998 (2016).
79. Fu, Y. *et al.* Broad wavelength tunable robust lasing from single-crystal nanowires of cesium lead halide perovskites ($CsPbX_3$, X = Cl, Br, I). *ACS Nano* **10**, 7963–7972 (2016).
80. Wang, Y. *et al.* Photon transport in one-dimensional incommensurately epitaxial $CsPbX_3$ arrays. *Nano Lett.* **16**, 7974–7981 (2016).
81. Ha, S. T. *et al.* Synthesis of organic–inorganic lead halide perovskite nanoplatelets: towards high-performance perovskite solar cells and optoelectronic devices. *Adv. Opt. Mater.* **2**, 838–844 (2014).
82. Wang, G. *et al.* Wafer-scale growth of large arrays of perovskite microplate crystals for functional electronics and optoelectronics. *Sci. Adv.* **1**, e1500613 (2015).
83. Chen, J. *et al.* Vapor-phase epitaxial growth of aligned nanowire networks of cesium lead halide perovskites ($CsPbX_3$, X = Cl, Br, I). *Nano Lett.* **17**, 460–466 (2017).
84. Zhou, H. *et al.* Vapor growth and tunable lasing of band gap engineered cesium lead halide perovskite micro/nanorods with triangular cross section. *ACS Nano* **11**, 1189–1195 (2017).
85. Liang, D. *et al.* Color-pure violet-light-emitting diodes based on layered lead halide perovskite nanoplates. *ACS Nano* **10**, 6897–6904 (2016).
86. Dou, L. *et al.* Atomically thin two-dimensional organic-inorganic hybrid perovskites. *Science* **349**, 1518–1521 (2015).
87. Chen, J. *et al.* A ternary solvent method for large-sized two-dimensional perovskites. *Angew. Chem. Int. Ed.* **129**, 2430–2434 (2017).
88. Akkerman, Q. A. *et al.* Tuning the optical properties of cesium lead halide perovskite nanocrystals by anion exchange reactions. *J. Am. Chem. Soc.* **137**, 10276–10281 (2015).
89. Koscher, B. A. *et al.* Surface- vs diffusion-limited mechanisms of anion exchange in $CsPbBr_3$ nanocrystal cubes revealed through kinetic studies. *J. Am. Chem. Soc.* **138**, 12065–12068 (2016).
90. van der Stam, W. *et al.* Highly emissive divalent-ion-doped colloidal $CsPb_{1-x}M_xBr_3$ perovskite nanocrystals through cation exchange. *J. Am. Chem. Soc.* **139**, 4087–4097 (2017).
91. Bischak, C. G. *et al.* Origin of reversible photoinduced phase separation in hybrid perovskites. *Nano Lett.* **17**, 1028–1033 (2017).
92. Dou, L. *et al.* Spatially resolved multi-color $CsPbX_3$ nanowire heterojunctions via anion exchange. *Proc. Natl Acad. Sci. USA* **114**, 7216–7221 (2017).
93. Caselli, D. A. & Ning, C. Z. High-performance laterally-arranged multiple-bandgap solar cells using spatially composition-graded $Cd_xPb_{1-x}S$ nanowires on a single substrate: a design study. *Opt. Express* **19**, A686–A694 (2011).
94. Caselli, D. A., Liu, Z. C., Shelhammer, D. & Ning, C. Z. Composition-graded nanowire solar cells fabricated in a single process for spectrum-splitting photovoltaic systems. *Nano Lett.* **14**, 5772–5779 (2014).
95. Caselli, D. A. & Ning, C. Z. Monolithically-integrated laterally-arrayed multiple bandgap solar cells for spectrum-splitting photovoltaic systems. *Prog. Quantum Electron.* **39**, 24–70 (2015).
96. Ning, C. Z.in *Semiconductors and Semimetals* Ch. 12 (eds Coleman, J. J., Bryce, A. C. & Jagadish, C.) (Academic Press, 2012).

97. Ma, Y., Guo, X., Wu, X., Dai, L. & Tong, L. Semiconductor nanowire lasers. *Adv. Opt. Photonics* **5**, 216–273 (2013).
98. Couteau, C., Larrue, A., Wilhelm, C. & Soci, C. Nanowire lasers. *Nanophotonics* **4**, 90–107 (2015).
99. Eaton, S. W., Fu, A., Wong, A. B., Ning, C. Z. & Yang, P. D. Semiconductor nanowire lasers. *Nat. Rev. Mater.* **1**, 16028 (2016).
100. Liu, C., Tang, J., Chen, H. M., Liu, B. & Yang, P. A. Fully integrated nanosystem of semiconductor nanowires for direct solar water splitting. *Nano Lett.* **13**, 2989–2992 (2013).
101. Liu, C., Dasgupta, N. P. & Yang, P. Semiconductor nanowires for artificial photosynthesis. *Chem. Mater.* **26**, 415–422 (2014).
102. Li, D. & Ning, C. Z. Electrical injection in longitudinal and coaxial heterostructure nanowires: a comparative study through a three-dimensional simulation. *Nano Lett.* **8**, 4234–4237 (2008).
103. Zhang, G., Tateno, K., Sogawa, T. & Nakano, H. Vertically aligned GaP/GaAs core-multishell nanowires epitaxially grown on Si substrate. *Appl. Phys. Express* **1**, 064003 (2008).
104. Duan, X., Huang, Y., Agarwal, R. & Lieber, C. M. Single-nanowire electrically driven lasers. *Nature* **421**, 241–245 (2003).
105. Fan, Z. *et al.* Three-dimensional nanopillar-array photovoltaics on low-cost and flexible substrates. *Nat. Mater.* **8**, 648–653 (2009).

Acknowledgements
C.-Z.N. acknowledges support from the 985 University Project of China, the Tsinghua University Initiative Scientific Research Program (No. 20141081296), and the ARPA-E MOSAIC Program (DE-AR001255-1527). C.-Z.N. thanks his students and postdocs over the past 10 years who have contributed to the study of semiconductor alloy nanomaterials, especially S. Amiri, D. Caselli, F. Fan, R. Liu, Z. Liu, P. Nichols, A. Pan, M. Sun, S. Turkdogan and L. Yin. L.D. and P.Y. are thankful for the support of the US Department of Energy, Office of Science, Basic Energy Sciences, Materials Sciences and Engineering Division under contract no. DE-AC02-05CH11231 (Physical Chemistry of Inorganic Nanostructures KC3103).

Author contributions
All authors contributed equally to the preparation of this manuscript.

Competing interests statement
The authors declare no competing interests.

Publisher's note
Springer Nature remains neutral with regard to jurisdictional claims in published maps and institutional affiliations.

How to cite this article
Ning, C.-Z., Dou, L. & Yang, P. Bandgap engineering in semiconductor alloy nanomaterials with widely tunable compositions. *Nat. Rev. Mater.* **2**, 17070 (2017).